D2.1 Description of the high-fidelity simulation

Date: April 11, 2024

Funded by
the European Union

This Project has received funding from the European Union's HORIZON Research and Innovation Programme under Grant Agreement number 101096698

Document Identification			
Status	Final	**Due Date**	31/03/2024
Version	1.0	**Submission Date**	12/04/2024

Related WP	WP2	**Document Reference**	D2.1
Related Deliverable(s)	D1.1	**Dissemination Level (*)**	PU
Lead Participant	KTH	**Lead Author**	Gerardo Zampino
Contributors		**Reviewers**	Elias Zea (KTH)
			Akshay Patil (TUD)

Keywords:
High-fidelity LES simulations, Turbulent boundary layer, Urban-like flow, Wall-mounted square cylinders

Document Information

List of Contributors	
Name	**Partner**
Gerardo Zampino	KTH
Federica Tonti	KTH

Document History			
Version	**Date**	**Change editors**	**Changes**
0.1	22/03/2024	Gerardo Zampino (KTH)	Writing the first draft of the deliverable
0.2	09/04/2024	Gerardo Zampino (KTH)	Writing the reviewed version of the deliverable addressing the reviewers' comments
1.0	11/04/2024	Gerardo Zampino (KTH)	Final Version

Quality Control		
Role	**Who (Partner short name)**	**Approval Date**
Deliverable leader	Gerardo Zampino (KTH)	11/09/2024
Quality manager	Gerardo Zampino (KTH)	11/09/2024
Project Coordinator	Ricardo Vinuesa (KTH)	11/09/2024

Table of Contents

2 Introduction.....8
2.1 Purpose of the document.....9
2.2 Relation to other project work.....9
2.3 Structure of the document.....10
3 Wake configuration description.....11
3.1 Isolated obstacle.....11
3.2 Two obstacles in tandem.....12
4 Simulation description.....13
4.1 Computational setup.....13
4.2 Boundary conditions.....14
4.3 Obstacle configurations.....15
5 Results regarding an isolated cylinder.....15
5.1 Effect of AR on the rear-wake.....15
5.2 Reynolds stress maps for a single obstacle.....19
5.3 TKE budget.....20
6 Two obstacles in tandem.....24
6.1 Effect of the gap between the buildings.....24
7 Training of the DLNN.....28
8 Conclusions.....29

List of Figures

Figure 1: Sketch of the numerical domain with a single obstacle.....14
Figure 2: Mean streamwise (left) and vertical (right) velocity components for the cases AR1 (a,b), AR2 (c,d), AR3 (e,f) and AR4 (g,h). The streamlines are shown on the left panels to help the reader to visualise the recirculation bubbles inside the wake.....16
Figure 3: Instantaneous vortical motions identified by 2 = −40 for the cases AR2 (top), AR3 (centre), AR4 (bottom). The colormap is the instantaneous streamwise velocity u, ranging from -1.1 (dark blue) to 1.75 (dark red). The arrow indicates the flow direction in each case.....
.....18
Figure 4: Summary of the wake configuration as a function of AR and Re from the present study (orange), Hosseini et al. [32] (magenta), Bourgeois et al. [33] (cyan), Sattari et al. [34] (purple), Vinuesa et al. [31] (black), Wang et al. [17],Uffinger et al. [35] (dark red), Yauwenas et al. [30] (dark magenta). In the figure, circle markers are

used for dipole wakes while cross markers refer to quadrupole wakes..... 19

Figure 5: turbulent kinetic energy at the symmetry plane z = 0 for the cases AR1 (panel a), AR2 (panel b), AR3 (panel c) and AR4 (panel d). The contour lines delimit the regions of high u'u' (yellow) v'v' (red) and w'w'(black)..... 20

Figure 6: production Pk (left column) and transport Tk (right column) terms of the turbulent kinetic energy budget for z=0. The cases AR1-AR4 are plotted from the top to the bottom panels..... 22

Figure 7: production Pk (left column) and transport Tk (right column) terms of the TKE budget for y=0.5. The cases AR1-AR4 are plotted from the top to the bottom panels..... 23

Figure 8: Comparison of the streamwise velocity components from the cases AR2 (left panel), SF, WI and IR (right panels). The streamlines are also reported for clarity. 25

Figure 9: Comparison of the streamwise velocity components from the cases SF21 (upper panels), WI21 (bottom panels). The streamlines are also reported for clarity. 26

Figure 10: turbulent kinetic energy at the symmetry plane z = 0 for the cases AR2, SF21 and WI21. The contour lines delimit the regions of high u'u' (yellow) v'v' (red) and w'w'(black)..... 27

Figure 11: Example of the optimum trajectory predicted by the NN for the case SF21. The green line delimits the starting point while the dark blue circle delimits the arriving region..... 29

List of Acronyms

Abbreviation / acronym	Description
ABL	Atmospheric Boundary Layer
DNS	Direct Numerical Simulation
DRL	Deep Reinforcement Learning
Dx.y	Deliverable number y belonging to WP x
EC	European Commission
GLL	Gauss–Lobatto–Legendre
IR	Isolated Roughness
LES	Large-eddy simulation
NN	Neural Network
RANS	Reynolds-Averaged Navier-Stokes
SEM	Spectral-Element Method
SF	Skimming Flow
UAM	Urban Air-Mobility
UAV	Unmanned Aerial Vehicles
WI	Wake Interference
WP	Work Package
ZPG	Zero-Pressure Gradient

Executive Summary

The study of the urban airflow and noise emissions is gaining importance for assessing the environmental impact of both drone and commercial flights. However, a comprehensive tool to evaluate and optimise flight trajectories for minimising environmental impact in terms of climate, local air quality, and noise is still missing in literature. In urban areas, understanding the urban flows is crucial for delineating high-risk zones around buildings and enhancing the efficient use of urban airspace by drones.

Numerical studies, in particular Reynolds-Averaged Navier-Stokes (RANS) simulations, have emphasised the importance of the urban layout on wind direction, heat diffusion, and pollutant dispersion. Nevertheless, RANS simulations may overlook the transient and unsteady nature of the flow structures around buildings, thus unsteady simulations are to be preferred. As part of RefMap, we applied high-fidelity simulations to predict the instantaneous flow field and statistical quantities in order to better understand turbulent structures around buildings and, thus, the riskiest regions that need to be avoided for safe UAV navigation. A simplified representation of urban areas can be sought through the use of square cylinders that represent bluff bodies subject to a turbulent boundary layer is investigated due to the large computational resources required to model a highly resolved flow around a realistic configuration. In addition, a very detailed analysis is necessary to describe the small-scale structures. Highly-resolved simulations have realistic turbulence predictions, providing valuable insights into the small-scale turbulence physics.

Despite the high computational costs, the high-resolution Large Eddy Simulations (LES) will be integrated with RANS-based simulations to develop a multi-fidelity framework that allows us to reduce the time consumption of the simulations and extend the predictive capabilities for drone trajectories across a large variety of realistic scenarios as part of Task 2.3.

2 Introduction

According to recent statistics, by 2030 more than 75% of the European population will reside in urban areas throughout the European Union (EU) [1]. The escalation of the urban population has many drawbacks, particularly concerning the higher pollution levels, which can negatively affect public health and the environment in general. Predicting turbulent flows around buildings dispersion becomes crucial for achieving Sustainable Development Goal 11 [2], which aims to make cities safe, sustainable, and inclusive. The LES simulations especially are the starting point for the analysis of the instantaneous wind loading on building facades where the turbulent small-scales are more relevant..

In the meanwhile, the recent development of electric and environmentally friendly transportation is expected to promote the use of unmanned aerial vehicles (UAVs) for goods delivery or other aims, resulting in an increase in urban air traffic. This requires a comprehensive examination of turbulence around buildings to optimise costs, trajectory planning, and mitigating potential collisions with the buildings.

Two main approaches have been published in literature, the first one concerning the detailed analysis of the turbulent structures within a turbulent boundary layer for a simplified configuration used to model the real-life buildings [3-16], the second one utilised a scaled version of the buildings for both experiments [17-18] and numerical simulations [19-21] to investigate the flow field in real-life configuration.

Regarding the first approach, the dispersion of pollutants [3-4], heat exchange mechanisms [5] and the wake turbulent structures have been extensively studied in the literature concerning urban-like configurations immersed in a turbulent boundary layer [6-8]. Recent experimental and numerical studies investigated the effect of the Reynolds number [9], cross-sectional shape [10], and boundary-layer thickness [11-12]. However, the dependence of the turbulent structures developing in the wake of a wall-mounted obstacle on its aspect ratio (AR) is not trivial [13-16]. The second approach is recommended when the objective is the study of a very specific case. For example, Lim and colleagues [17] studied the transport of pollutants throughout a suburban area of Southampton (UK) using an in-scale 3D printed model of the city placed in a water tunnel. Bitter and Hanna [22] explored the pollution transport within urban environments and concluded that the buildings' shapes and distribution, the different heights of the houses, the presence of parks or trees can affect the propagation of the pollutant throughout the cities and their effect is not negligible. Nevertheless, real-life measurements [23] are expensive and less practical alternatives to the numerical simulations. In the last decades, many authors developed LES codes to study atmospheric boundary layers (ABL) impacting at-scale buildings and cities [19-21]. uDALE [19, 24-25], DALES [26] and FastEddy [27] are only examples of the large variety of softwares available in literature. A

detailed review of the methodologies used for the simulations of ABL in urban environment has been reported by García-Sánchez [28]

Although these softwares employs LES to resolve the turbulent flow around real-shaped buildings [17, 25], the coarser resolution compared with the aforementioned DNS or LES carried out for a simplified configuration does not allow resolving the small turbulent scales that become important in the context of RefMap when considering UAV. The vortex configuration plays an important role in shaping the production and distribution of the wake turbulence [16]. Therefore, a thorough understanding of this phenomenon is essential for avoiding high-risk regions characterised by elevated turbulence levels, which may negatively impact drone flight performance.

2.1 Purpose of the document

The impact of wind velocity and turbulent structures within urban environments significantly impacts the energy consumption and safety of drones engaged in city operations for the movement of goods or other services. The real-time estimation of the drone trajectories is crucial to mitigate risks of accidents and damages to drones, goods and people. This task is under development in the WP3, Task 3.3, which aims to employ a deep reinforcement learning (DRL) method to train a neural network for optimal trajectories in cities and urban environments.

Within this framework, high-fidelity simulations are the benchmark configuration and reference case for training the aforementioned neural network. In fact, we need an accurate simulation of the spatio-temporal evolution of the turbulent flow around the buildings. The main objective of this deliverable is to present the mathematical framework of the simulation software used for analysing turbulent flow structures. In this context, task 2.1 aims to provide the benchmark data that will be used by the WP3 for the development of the neural network. This will address the requirement to transform the digital aviation technologies for Urban Air-Mobility (UAM) with minimal environmental impact.

2.2 Relation to other project work

The high-fidelity simulations have been designed to replicate a simplified urban configuration represented as bluff bodies using square cross-sections. The present results are used for the multi-fidelity framework in WP2 that seeks to examine the impact of the incoming flow using RANS simulations or other low-fidelity frameworks. The outcomes from the high-fidelity simulations are thus used for two different purposes:

- To train and validate the DRL neural networks outlined in WP3
- To explore the multi-fidelity framework possibilities from WP2 for the analysis of turbulent flows around bluff body objects in a turbulent boundary layer

2.3 Structure of the document

This document is structured in 6 major chapters:

Chapter 3 describes the computational setup of the high-resolution LES that contains the definition of the numerical domain and the boundary conditions;

Chapter 4 summarises the most recent numerical and experimental studies regarding the turbulent structures in the wake of an isolated wall-mounted cylinder and two obstacles in tandem;

Chapter 5 reports the most interesting results divided between the cases with a single obstacle and two obstacles in tandem;

Chapter 6 reports the most interesting results divided between the cases with a single obstacle and two obstacles in tandem;

Chapter 7 summarises how the present data are used to DRL methods

Chapter 8 reports the conclusions;

3 Wake configuration description

3.1 Isolated obstacle

Before presenting the most interesting findings of the present analysis concerning a single square cylinder, it is worth providing a summary of the most common model of near-wake turbulent structures. Wang and Zhou [29] proposed an empirical interpretation of the turbulent wake as the synthesis of three structures: tip, base and spanwise vortices. Tip vortices, as defined by Wang and Zhou [29], consist of a couple of counter-rotating vortices emerging at the free end of the cylinder roof. These vortices induce a strong downwash in the wake, easily displayed in the mean streamwise velocity plot. In proximity to the base, another pair of counter-rotating vortices develop with an opposite sense of rotation with respect to the tip vortices. These base vortices are inclined upwards and generate a significant upwash in the lower portion of the wake. Both tip and base vortices extend downstream of the cylinder in the streamwise direction and are employed by Wang and Zhou [29] to differentiate between a “dipole”, characterised by only tip vortices, and “quadrupole” wake, where both tip and base vortices are present.

The third structures are the so-called spanwise vortices, defined as turbulent structures separating from the flanks of the cylinders. Sakamoto and Arie [30] hypothesised that the flow detaching from the cylinder’s upper surface generates a turbulent filament that bridges the spanwise vortices emerging from the flanks of the cylinder. Sumner et al. [31] interpreted the base vortices as the oblique separation of the spanwise vortices. As a consequence, the spanwise vortices are inclined upwards and they are streamwise-developing rolls. Following these assumptions, Wang and Zhou [29] speculated that the spanwise vortices on the cylinder’s sides consist of two vertical turbulent filaments that are linked to each other by a horizontal bridge forming an arch-type vortex.

Hence, the spanwise vortices may exhibit either symmetric arranged (symmetric wake) or staggered (antisymmetrical or Kármán vortex shedding). The tip and base vortices are the footprint in a vertical section of the arch-type vortex theorised by Sakamoto and Arie [30].

Furthermore, Rastan et al. [32] introduced a conceptual model to elucidate the impact of the cross-section aspect ratio (CR) on the flow separation and wake characteristics, using both numerical and experimental setups. Here, CR denotes the ratio between the cylinder’s longitudinal length and width. Rastan et al. [32] observed that CR affects more significantly the wake structures compared to AR and for CR=1

the wake features two streamwise vortices originating from the lateral edges, forming a dipole configuration.

Here, the present document aims to understand the generation physics of the near-wake turbulent structures that are strongly affected by small scales [33-34] which RANS cannot resolve. In addition, LES and DNS provide unsteady features of the wake that are pivotal for the aforementioned study of the drone optimal trajectories.

3.2 Two obstacles in tandem

A single obstacle is not accurate enough to study the urban-like flow, as both experiments and simulations often overlook the iterations between buildings. While numerous experiments have been conducted to explore pedestrian comfort [35], pollutant dispersion [3-4], and the extension of the urban heat island [5] in realistic urban flows, such experiments are expensive and limited to very specific scenarios. Numerical simulations are either infeasible due to the larger domain size or high order of details necessary for the simulation of real-life cities.

In numerical simulations an array of wall-mounted cylinders is hence preferred [33-34]. A summary of the available simulations in literature has been published by Atzori et al. [16]. In the present document, we limit our analysis to the case of two buildings of different heights in tandem in order to investigate the interaction between the wall-mounted cylinders with different heights. This study is motivated by the fact that buildings in real-life cities have different sizes and heights.

The interaction between two buildings in a row has been first investigated by Oke [7] who distinguished into three different configurations as a function of the distance: (i) Skimming Flow (SF), observed for narrow streets where the flow skims above the street and the wake of the leading obstacle is significantly affected by the rear one; (ii) Wake Interference (WI), occurring in larger gaps where the flow penetrates within the street and wakes of both obstacles interact; (iii) Isolated Roughness (IR) case where the wake of the upfront obstacle is unaffected by the presence of the second obstacle. In their paper, Atzori et al [16] utilised the Reynolds number based on the free-stream velocity and obstacle height is $Re_h = 10\,000$, with $Re_\tau = u_\tau \delta/\nu \cong 175$ prior to the first obstacle[1]. Three different configurations were considered by Atzori et al. [16], corresponding to the three different flow regimes identified in the literature. In the SF regime, a little penetration occurs from the free stream into the cavity between the two obstacles, with the wake of the leading obstacle overwhelming the second

[1] Note that in [16] the definition of the friction Reynolds number is inexact since it accounts for the height h rather than δ.

obstacle [16]. In the WI regime, strong interactions arise between the free stream and the wake of the leading obstacle [16]. In the IR regime, the wake behind remains largely unaffected by the presence of the second obstacle [16].

We refer to Atzori et al. [16] for the analysis of the wake structures generated by two cylinders in tandem with the *same* height. In the present study, we examine the turbulent wake for two wall-mounted cylinders in tandem with *different* heights.

4 Simulation description

The present study is primarily motivated by the lack of high-resolution LES investigating the turbulent structures developing in the wake of a wall-mounted square cylinder immersed within a turbulent boundary layer (BL) with large thickness, as commonly encountered in modelling an atmospheric boundary layer in urban environments. The resolution employed in the present analysis is slightly coarser than those in DNS [16], and at relatively high Reynolds numbers.

4.1 Computational setup

The computational domain for a single wall-mounted cylinder is reported in Figure 1. The flow field is is decomposed into the instantaneous streamwise u, vertical v and spanwise w velocities along the x, y, and z axes, respectively. The governing equations are normalised by the height of the cylinder h and by the free-stream velocity u_∞ of the incoming flow. Given these definitions, the simulations are carried out for Reynolds number $Re_h = u_\infty h/\nu = 10000$, where ν is the kinematic viscosity. Upfront the first obstacle, the friction Reynolds number $Re_\tau = u_\tau \delta/\nu$ is approximately 170, where δ is the boundary-layer thickness, and it is fixed for all cases considered in this document. Finally, we define the momentum-thickness-based Reynolds number as $Re_\theta = u_\infty \theta/\nu = 490$ upfront the first obstacle, where θ denotes the momentum thickness. The domain size is $L_{x_1} = 10h$, $L_{x_2} = 6h$, $L_y = 3h$, and $L_z = 4h$ in the x, y, z directions, respectively.

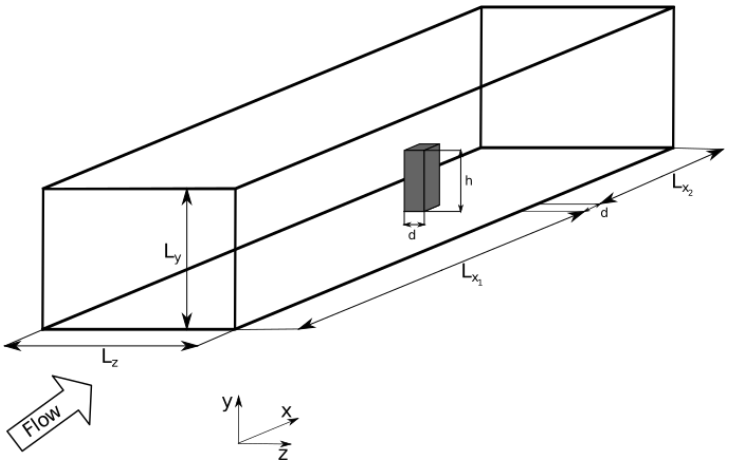

Figure 1: Sketch of the numerical domain with a single obstacle

All simulations were conducted using the open-source code Nek5000, which was developed by Fischer et al. [36]. Nek5000 employs the spectral-element method (SEM) described by Patera [37]. This method aims to approximate the solutions of the momentum equations on a finite volume element using a polynomial discretization based on the Gauss–Lobatto–Legendre (GLL) quadrature method. Specifically, Nek5000 employs the $P_n - P_{n-2}$ formulation of the Galerkin projection method, where n denotes the maximum polynomial order of the trial function for the velocity, while $n-2$ corresponds to the polynomial order for the pressure trial function.

To enhance the accuracy of the high-resolution LES two strategies are equally possible: (i) increasing the number of mesh elements in proximity of the wall to better resolve the inner BL; (ii) increasing the order of GLL polynomials to increase the resolution across the entire mesh. For the RefMap project, the former strategy has been adopted. The total number of mesh elements ranges 210,000 to 240,000 with a 7th-order GLL polynomial for all cases considered. The mesh follows the criteria proposed by Negi et al. [38] for the high-resolution LES implementation. Thus, in the near-wall region, the resolution follows the guidelines $\Delta x^+ < 18$, $\Delta y^+ < 0.5$ and $\Delta z^+ < 9$ [16]. Away from the wall, the mesh resolution satisfies the condition $\Delta/\eta < 9$, where $\Delta = (\Delta x \Delta y \Delta z)^{1/3}$, $\eta = (\nu^3/\epsilon)^{1/4}$ is the Kolmogorov scale and ϵ denotes the local isotropic dissipation.

4.2 Boundary conditions

No-slip boundary conditions are enforced at the wall and on the surfaces of the obstacles. At the inlet, we impose a laminar Blasius boundary layer profile with a displacement-thickness-based Reynolds number $Re_{\delta^*}=450$. Numerical tripping is utilised to induce the transition from laminar to turbulent flow. This involves a

numerical forcing in the transversal direction at $x=-9$ in agreement with the experimental tripping [16]. At the outlet, the stabilised condition from Dong et al. [39] is employed. On the upper boundary, we impose an uniform freestream velocity and a non-zero outflow velocity to set a zero-pressure-gradient (ZPG) boundary layer.

4.3 Obstacle configurations

For all cases detailed in this document, the square cylinder has a unitary height $h=1$ and a square cross-section with width d. Here, the aspect ratio (AR) is defined as the ratio of the obstacle height to its width $\mathrm{AR}=h/d$.

Two configurations have been primarily studied:

1. a single obstacle with varying aspect ratio ranging from 2 to 4. Each case is referred to as ARx where x is the corresponding AR value.
2. two obstacles displaced in a row.In this setup, the height of the upfront cylinder is unitary while the rear obstacle has half the height. The distance between the two obstacles is scaled with the height of the upfront cylinder. Thus, the gap between the two cylinders varies from 1.5 to 2.5, corresponding to the skimming flow (SF) and wake interference (WI) as reported by Atzori et al. [16]. These cases are denoted as SF21 and WI21. The case corresponding to the isolated roughness (IR21) is still running.

5 Results regarding an isolated cylinder

5.1 Effect of AR on the rear-wake

Despite the well-established understanding of the impact of Aspect Ratio (AR) on the near wake documented in the literature [9,13, 14, 32], the major part of numerical simulations published are conducted at a lower Reynolds number or with a lower resolution than the present analysis. We aim to investigate the influence of the AR on the turbulent vortical structures in the rear-wake region employing wall-resolved LES with higher resolution than the most common LES techniques proposed in literature. The resolution increase is due to the use of spectral methods applied to every element of the mesh, producing a local increase of the mesh resolution, which is the underlying idea of the SEM method [37]. For this reason, throughout the entire document we refer to these simulations as “high-resolution LES”.

Mean streamwise and vertical velocities in the symmetric plane are depicted in the left and right columns of Figure 2, respectively. The effect of the AR on the size of the recirculation region in the wake is investigated. The streamlines are also displayed in the same figure to help the reader visualise the mean wake structures. For the case

AR1 (panel a), the wake displays weak tip vortices and no base vortices. The recirculation region extends for the entire height of the obstacle. As AR increases, the wake stretches in both spanwise and streamwise directions. The tip vortices increase in strength, producing a stronger

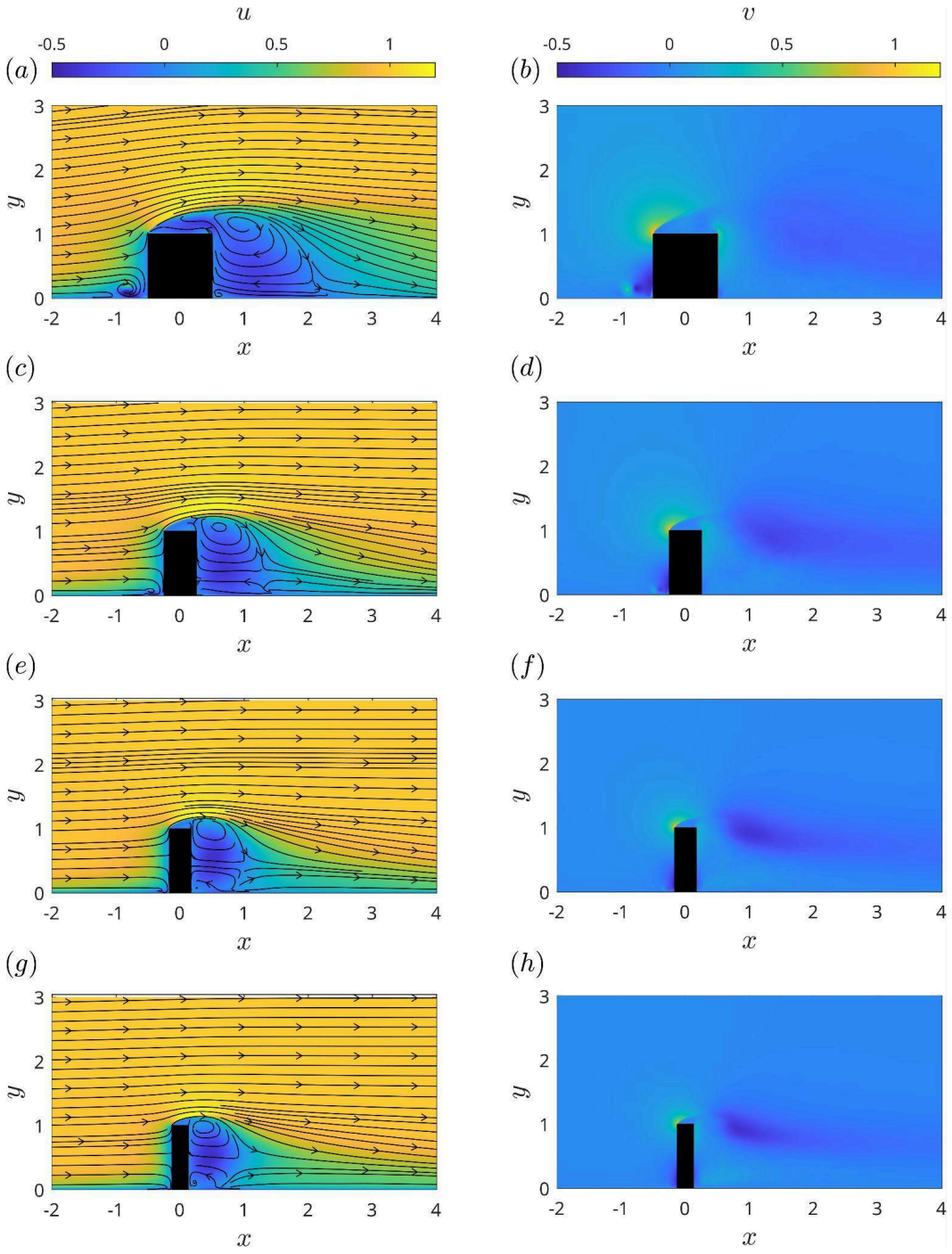

Figure 2: Mean streamwise (left) and vertical (right) velocity components for the cases AR1 (a,b), AR2 (c,d), AR3 (e,f) and AR4 (g,h). The streamlines are shown on the left panels to help the reader to visualise the recirculation bubbles inside the wake

downwash motion. Consequently, the recirculation zone reduces in size and the base vortices produce a secondary recirculation bubble at the bottom half of the wake. For AR2–AR4, the flow reattachment on the roof is prevented due to the lower width of the cylinder. In front of the obstacle, a horseshoe vortex emerges. with its size varying inversely with AR, disappearing entirely in AR4 as it merges with base vortices. The horseshoe vortex envelops the sides of the obstacles, causing a downward flow within the vertical tails on either side of the obstacle.

Zhang et al. [40] used the impingement point to describe the changes of the wake due to the occurrence of the base vortices at higher AR (see panels f and h). Here, the impingement point is defined as the saddle point where both the upwash and downwash coexist. For AR1, the impingement point lies at the bottom wall. However, when increasing AR (panels e and g), the impingement point moves away from the wall, indicating that the base vortices are developing behind the obstacle. A similar change in the wake configuration has been observed by Zhao et al. [9], who carried out a series of simulations of square wall-mounted cylinders for a fixed AR and at increasing Re_h.As the Reynolds number increases, the impingement point moves from the centre of the wake (for $Re_h = 100$) to the wall (for $Re_h = 500$) and the wake of the wall-mounted cylinder changes. This similarity between the present analysis and the cases in [9] suggests that both the turbulence characteristics of the incoming boundary layer and the AR are equally important to describing the evolution of the near-wake.

The difference in the mean velocity can be explained also by considering the instantaneous field in Figure 3. The main vortical structures are identified using the λ_2 -criterion. The wake is symmetric only for the case AR1 (not shown) and AR2. For AR3 and AR4, the wake is antisymmetric due to the Kármán vortex shedding. In panels (b) and (c), base vortices are discernible, the flow is a quadrupole and the turbulent structures are aggregated into more complex structures. In this framework, Dousset and Pothérat [41] distinguished between a symmetric shedding ($Re_d = u_\infty d/\nu = 200$), where a single row of the hairpin vortices is aligned in the streamwise direction, and antisymmetric vortex shedding ($Re_d > 250$), where the upwash induced by the base vortices forces the hairpin vortices to aggregate into a more complex turbulent structure. However, our simulations depict a more chaotic wake, with the arch-type vortex separating at the cylinder edges being the only preserved pattern across all the cases.

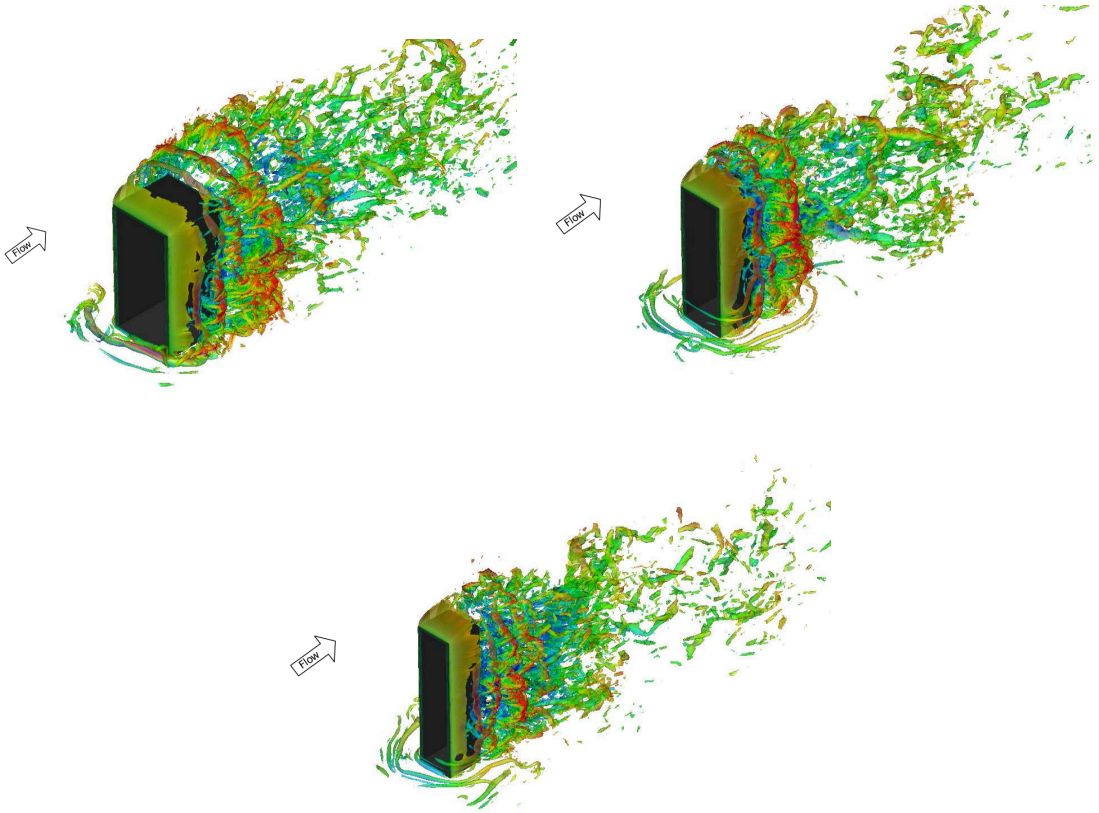

Figure 3: Instantaneous vortical motions identified by λ_2 = −40 for the cases AR2 (top), AR3 (centre), AR4 (bottom). The colormap is the instantaneous streamwise velocity u, ranging from -1.1 (dark blue) to 1.75 (dark red). The arrow indicates the flow direction in each case.

Based on the instantaneous field, our analysis reveals that the critical aspect ratio (AR_c) lies between 2 and 3, where the wake loses its symmetry. The critical aspect ratio depends on a series of parameters, such as the momentum thickness θ, the boundary-layer thickness δ, and the turbulence properties of the incoming boundary layer. In the present investigation, we propose a qualitative description of the transition between dipole and quadrupole wakes, say theAR_c, as a function of Re_θ. Here, the momentum thickness is preferred because it accounts for both boundary-layer thickness and the turbulent properties of the incoming boundary layer. In Figure 4 the wake configuration is depicted as a function of Re_θ. Circular markers denote dipole configurations while cross markers are used for quadrupole wakes. We distinguish between the dipole-wake region in blue, and the quadrupole-wake region in red. These regions exhibit an overlap within the transition region. In their paper, Yauwenas et al. [42] observed that dipole and quadrupole configurations are equally possible inside the transition region. However, Yauwenas et al. [42] addressed the dependence on boundary-layer thickness, neglecting the turbulence properties of the flow. We denoted that the only boundary-layer thickness

is inadequate to characterise the transition between the symmetric and antisymmetric wakes [42]. As discussed by Vinuesa et al. [43], the turbulence characteristics of the incoming flow can alter the wake configurations, also explaining the discrepancy between the present data and the results produced by Yauwenas et al. [42]. However, the lack of data within the transition region makes it difficult to establish the exact extension of this area. The dependence of the ARc on the Reynolds number is well-known in the literature. Within a moderate range of Re_θ between 480 and 800, the ARc increases and its value is between 2–6. For lower Re_θ between 100 and 400, the critical value rapidly decreases and the dipole wake has been observed experimentally for very large AR [44]. On the other hand, AR_c peaks at 5.5 for $Re_\theta = 809$, and a further increase of Reτ produces a reduction of AR_c that needs to be evaluated.

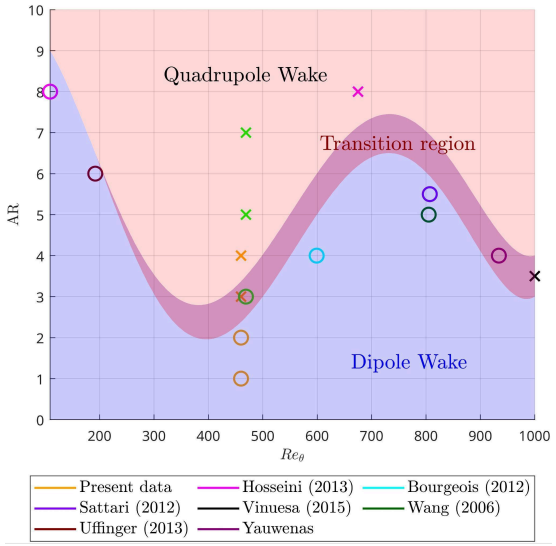

Figure 4: Summary of the wake configuration as a function of AR and Re_θ from the present study (orange), Hosseini et al. [32] (magenta), Bourgeois et al. [33] (cyan), Sattari et al. [34] (purple), Vinuesa et al. [31] (black), Wang et al. [17],Uffinger et al. [35] (dark red), Yauwenas et al. [30] (dark magenta). In the figure, circle markers are used for dipole wakes while cross markers refer to quadrupole wakes

5.2 Reynolds stress maps for a single obstacle

Due to the three dimensionality of the wake-flow, the turbulent energy is not equally distributed across the three reference directions. The turbulent kinetic energy (TKE) is given by $1/2\ (\overline{u'u'} + \overline{v'v'} + \overline{w'w'})$ in the longitudinal symmetric plane ($z=0$) is firstly plotted in Figure 5. The peak region of $\overline{u'u'}$, $\overline{v'v'}$ and $\overline{w'w'}$ are reported in the same figure, displaying a correlation with the TKE peak. Before the cylinder, the high TKE corresponds to the horseshoe vortex, whose size and position depend on the AR. In particular, for the cases AR1 (panel a) and AR2 (panel b), the horseshoe vortex is more prominent due to a stronger adverse pressure region in front of the cylinder. As

AR increases (panels c and d), the adverse pressure diminishes and the separation region moves towards the upfront surface of the building. Consequently, the horseshoe vortex diminishes in size, becoming negligible for AR3 (panel c) and AR4 (panel d). The streamwise component $u'u'$ (yellow line) is the dominant contributor to turbulence fluctuation, with other components being negligible or approaching zero. Within the wake, a third, weaker peak is observed in the upper part. This peak aligns with the peak region of $\overline{u'u'}$ (yellow line), $\overline{v'v'}$ (red line), and $\overline{w'w'}$ (black line). This disparity in turbulence energy can be attributed to variations in wake configurations. For AR1 (panel a) and AR2 (panel b), the wake exhibits a dipole structure, with the primary vortex being the arch-type vortex located above the cylinder, serving as the source of turbulence. For the AR3 (panel c) and AR4 (panel d), the peak moves inside the wake region. Similarly, the regions of high $\overline{u'u'}$ above the obstacles are reduced, i.e. the wake is affected by a very strong downwash due to the tip vortices, which transports the high-energy flow in the outer part of the boundary layer towards the low-momentum flow regions.

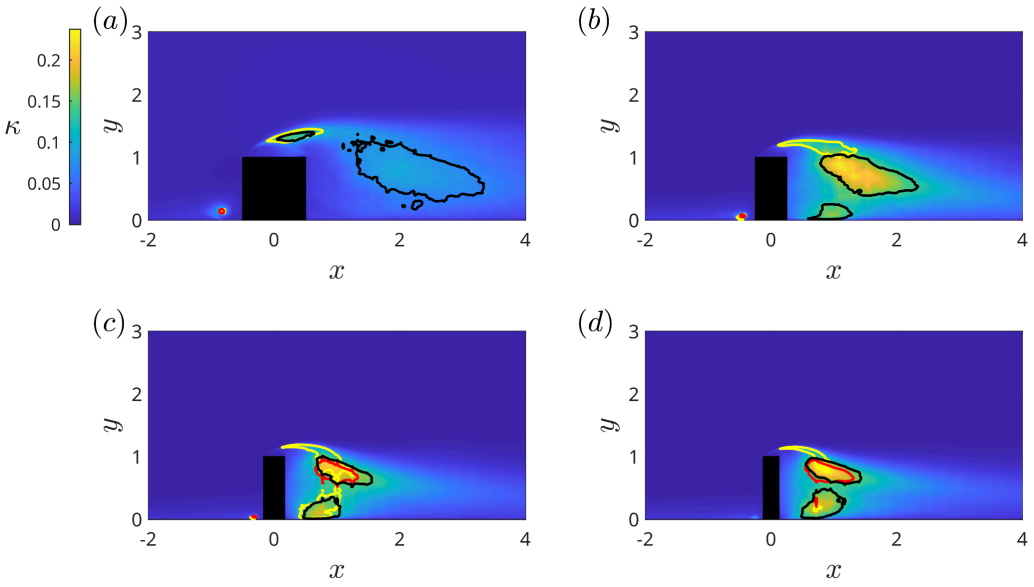

Figure 5: turbulent kinetic energy at the symmetry plane z = 0 for the cases AR1 (panel a), AR2 (panel b), AR3 (panel c) and AR4 (panel d). The contour lines delimit the regions of high $\overline{u'u'}$ (yellow) $\overline{v'v'}$ (red) and $\overline{w'w'}$(black).

5.3 TKE budget

The effect of the AR on the TKE budget is finally reported. The transport equation of the Reynolds-stress tensor is:

$$\frac{\partial}{\partial t}\overline{u_i'u_j'} = \underbrace{-\overline{u_i'u_k'}\frac{\partial u_j}{\partial x_k} - \overline{u_j'u_k'}\frac{\partial u_i}{\partial x_k}}_{P_{ij}} \underbrace{-2\nu\overline{\frac{\partial u_i'}{\partial x_k}\frac{\partial u_j'}{\partial x_k}}}_{\epsilon_{ij}} + \underbrace{\nu\frac{\partial^2}{\partial x_k^2}\overline{u_i'u_j'}}_{D_{ij}} \underbrace{-\frac{\partial}{\partial x_k}\overline{u_i'u_j'u_k'}}_{T_{ij}} + \underbrace{u_k\frac{\partial}{\partial x_k}\overline{u_i'u_j'}}_{C_{ij}} +$$
$$\underbrace{-\frac{1}{\rho}\left(\overline{p\frac{\partial u_i'}{\partial x_j}} + \overline{p\frac{\partial u_j'}{\partial x_i}}\right)}_{\Pi_{ij}^s} \underbrace{-\frac{1}{\rho}\left(\frac{\partial}{\partial x_j}\overline{pu_i'} + \frac{\partial}{\partial x_i}\overline{pu_j'}\right)}_{\Pi_{ij}^t},$$

where P_{ij} is the production term, ϵ_{ij} is the pseudo dissipation term, D_{ij} refers to the viscous diffusion, T_{ij} refers to the turbulent transport while C_{ij} is the convection term. The pressure strain and the pressure transport are denoted by $\Pi_{ij}^{\ s}$ and $\Pi_{ij}^{\ t}$. Given the definition of TKE, the Reynolds-stress equation becomes

$$\frac{\partial k}{\partial t} = P^k + \epsilon^k + D^k + T^k - \Pi^k - C^k,$$

where each term with superscript ^k is the trace of the corresponding tensors on the right-hand side of the TKE equation. The production P^k and the transport T^k at the vertical symmetry plane are shown in Figure 6 from AR1 (top panels) to AR4 (bottom panels). For brevity, the remaining terms of the TKE budget are omitted from the discussion. The yellow and black lines in the figure correspond to the peak of the normal stress $\overline{u'u'}$ and TKE, respectively. From the figure, it is evident that both P^k and T^k are significant only in the proximity of the obstacles where the production term exhibits four strong regions: three within the symmetry plane and one within the horizontal plane (see Figure 7). The size of these regions varies with the aspect ratio (AR). The regions are: (i) at the roof of the wall-mounted cylinder in the flow separation region, (ii) ahead of the obstacle in correspondence with the horseshoe vortex, (iii) in the lower part of the wake and (iv) along the flank of the cylinder. For the case AR1 (panel a) the production term peaks above the obstacle, rapidly diminishing inside the wake where it assumes a weak positive value. When the AR increases, the peak P^k region is distorted and deflected towards the centre of the wake while the peak corresponding to the horseshoe vortex moves downstream. For the cases AR3 (panel e) and AR4 (panel g) a weak positive region is observed at the bottom surface due to the presence of the base vortices.Despite turbulence production being concentrated above the cylinders for lower aspect ratios, the wake becomes the primary region of maximum turbulent production as AR increases. As observed in Figure 6, the upper portion of the wake captures the high-energetic flow of the outer part of the boundary layer. Similarly, at the bottom surface the flow is pushed upward towards the wake core due to the base vortices. As a consequence, the wake emerges as the principal region of turbulence production.

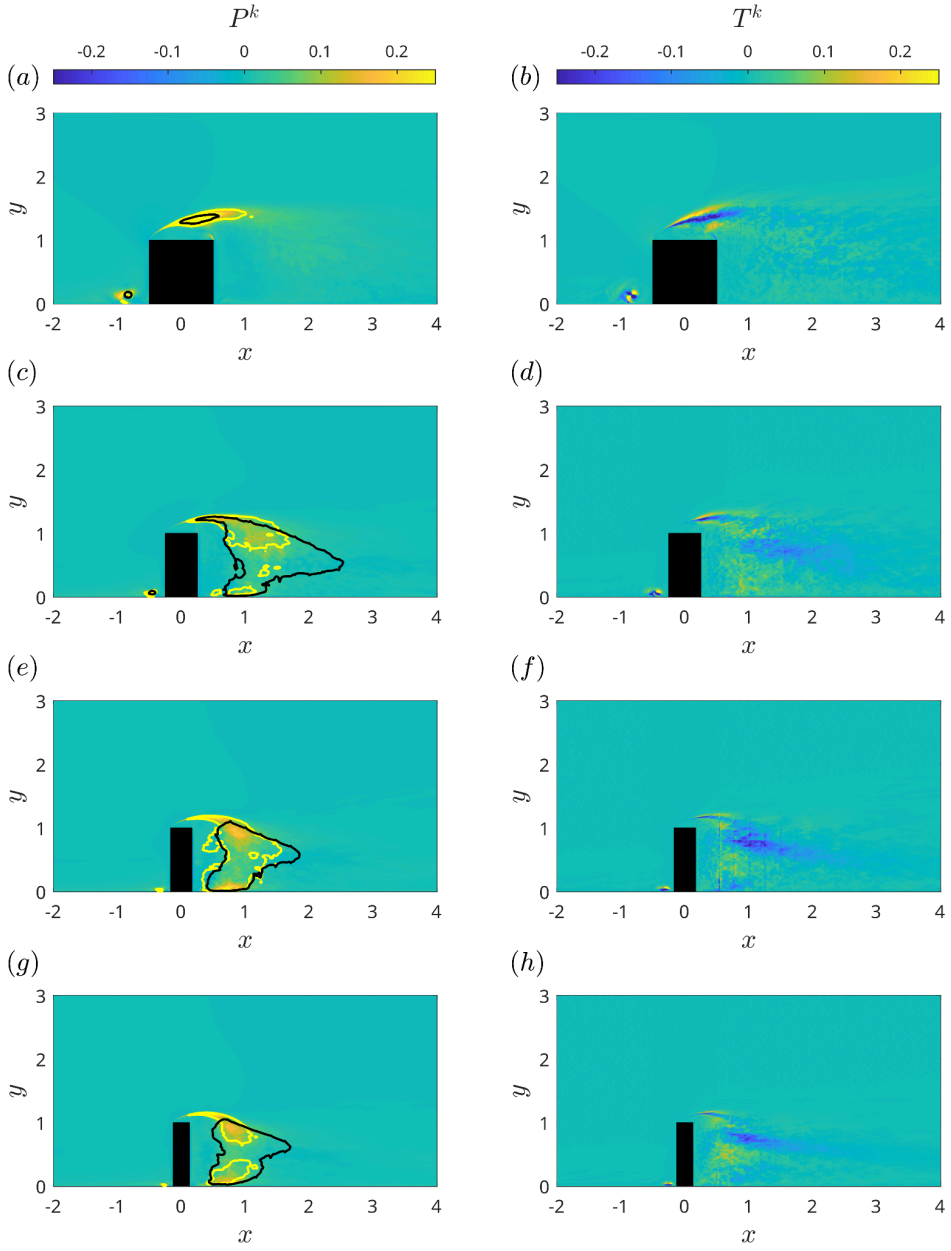

Figure 6: production P^k (left column) and transport T^k (right column) terms of the turbulent kinetic energy budget for $z = 0$. The cases AR1-AR4 are plotted from the top to the bottom panels.

The transport term T^k is also displayed in the right column of Figure 6. The map of T^k shows a positive/negative pattern above the obstacle while the transport term is weak and negligible inside the wake. In correspondence with the horseshoe vortex,

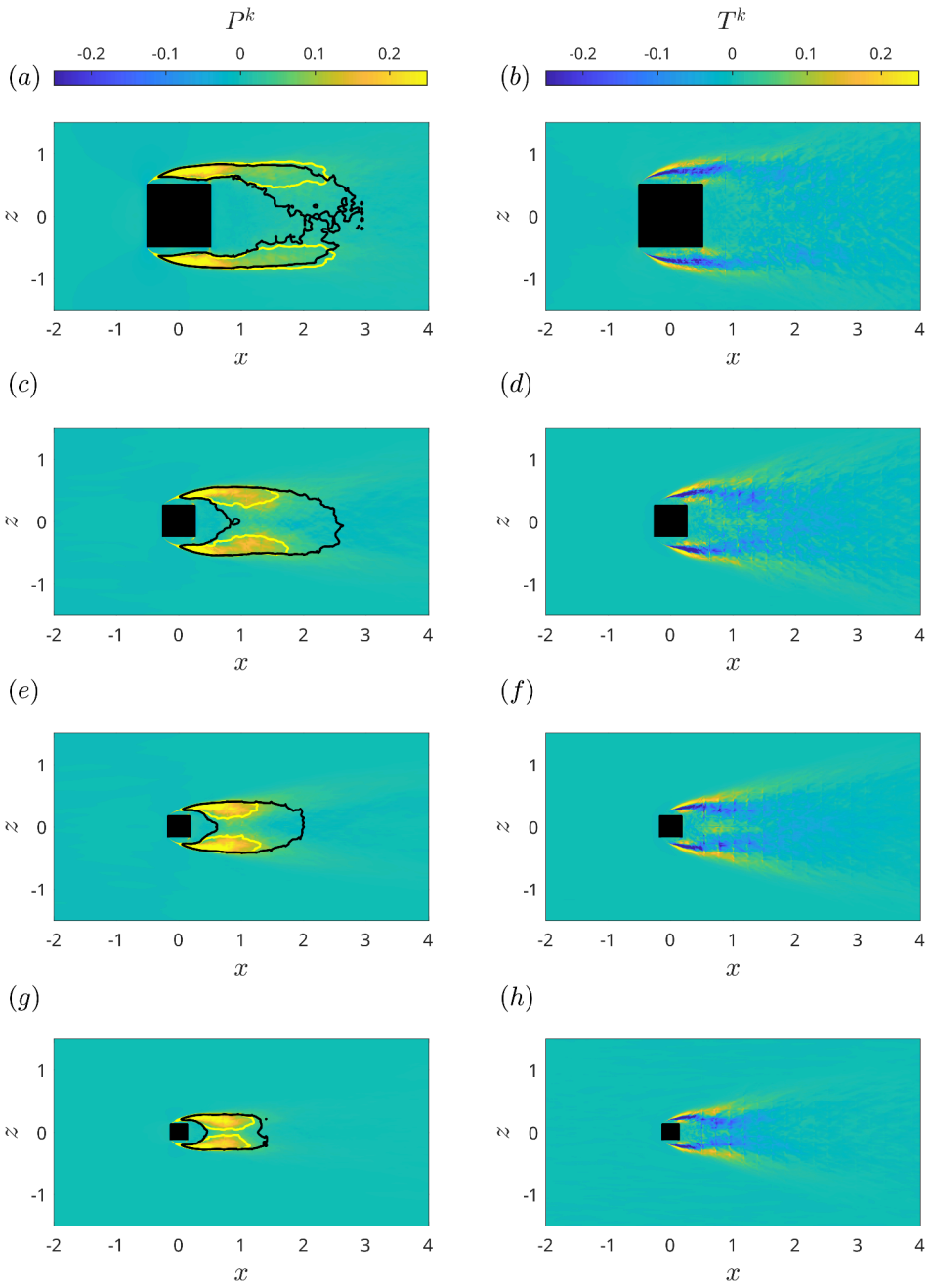

Figure 7: production P^k (left column) and transport T^k (right column) terms of the TKE budget for $y = 0.5$. The cases AR1-AR4 are plotted from the top to the bottom panels.

the transport term has alternative positive/negative turbulence transport. Comparing the left panels to the increasing aspect ratio (AR) produces a deformation of the region of negative T^k that extends into the wake behind the obstacle. For the sake of completeness, the P^k and T^k in the horizontal plane z=0.5 are finally reported in

Figure 7. The figure displays a region of high turbulent production that is not symmetric as expected even if the code largely converged. The discrepancy between the upper and lower portion of the figure is otherwise negligible and can be adduced to the coarser mesh in the wake of the buildings. The turbulence produced within this region is then transported inside the wake by the transport term that shows a positive/negative pattern. For the cases AR2 (panel c) to AR4 (panel g), the positive regions of P^k are deflected from the flank towards the wake centre. Similarly, the term T^k has two peak regions at the flank of the obstacles, while for increasing aspect ratio, the wake displays a negative transport term. The case AR1 is the only one that does not display positive production in the wake because it is the only case where the flow reattaches at the roof, the tip vortices are less intense, and their influence on the wake is weak. On the contrary, for the cases AR3 and AR4, the tip and base vortices are stronger, mainly impacting on the turbulence generation inside the wake. From a physical standpoint, the analysis of the TKE budget corroborates the idea that turbulence is initially generated in the flow-separation region and is subsequently transported into the wake.

6 Two obstacles in tandem

6.1 Effect of the gap between the buildings

In Figure 8, we compare the streamwise velocity component of the case AR2 and the two-tandem buildings configuration at different gaps, ranging from skimming flow (SF) to isolated roughness (IR), as recently reported by Atzori et al. [16]. Streamlines are provided for clarity to highlight the recirculation regions inside the wake. The incoming turbulent flow remains consistent across all cases investigated in this study. Thus, the horseshoe vortex observed upstream of the first cylinder remains unaltered and unaffected by the proximity of the second cylinder. For the case AR2, the wake extends downstream by a quantity equal to barely twice the cylinder height. We can distinguish between two recirculation regions: one in the upper portion of the wake delimited upwards by the tip vortices, and a second recirculation region in the lower half of the wake. As extensively described by Atzori et al. [16], in the skimming flow case (SF), the second obstacle significantly constrains the development of the wake. When compared to the case AR2, the lower vortex disappears. The outer layer flow does not penetrate between the cylinders; instead, it reattaches at the frontal edge of the second cylinder. The gap between the obstacles is entirely occupied by the recirculation bubble. A less intense recirculation region is observed behind the second obstacle while it extends for the entire height of the obstacle. Due to the proximity of the second obstacle, the wake of

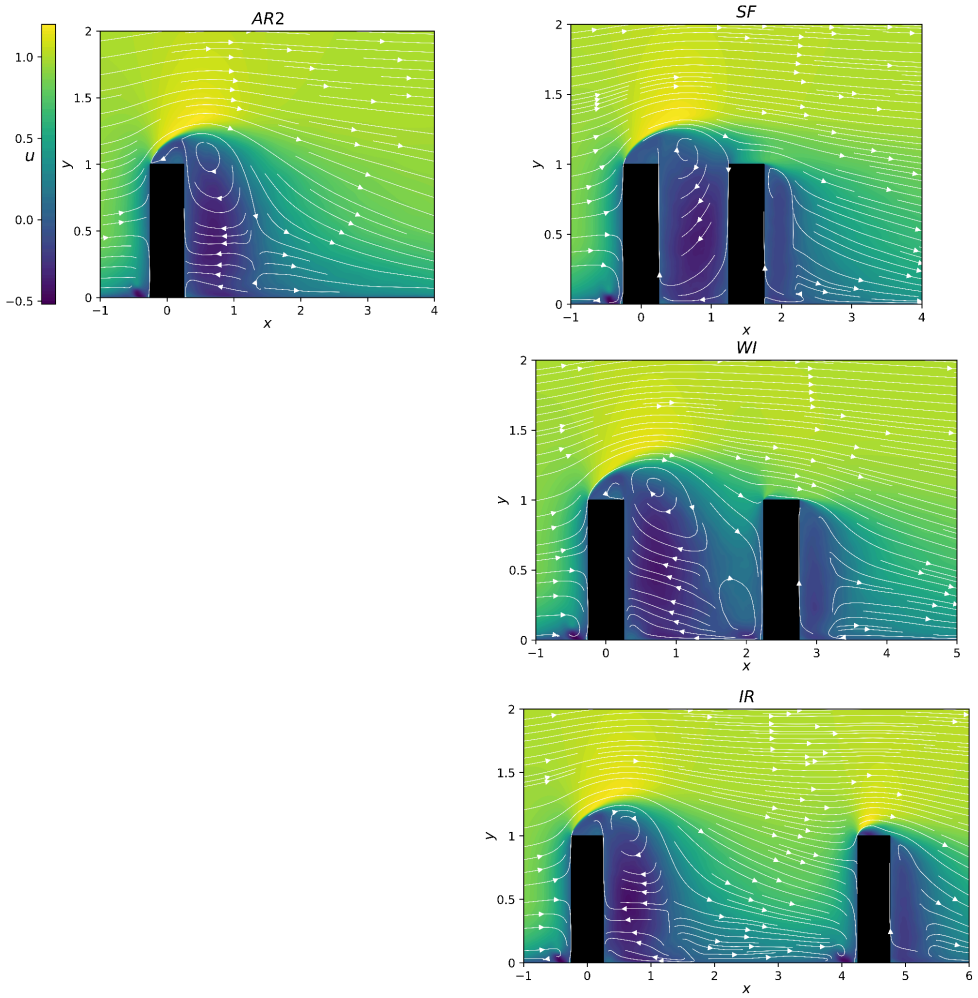

Figure 8: Comparison of the streamwise velocity components from the cases AR2 (left panel), SF, WI and IR (right panels). The streamlines are also reported for clarity.

the leader obstacle propagates behind the second obstacle, which mitigates the downwash effect behind the rear cylinder. However, with an increasing gap (case WI), the outer-layer flow penetrates between the obstacles. The flow reattaches at the leading face of the second cylinder, creating an additional low-velocity zone in front of the second obstacle. As in the case IR, this region diminishes in size and strength with the gap. For the IR case the downwash induced by the tip vortices between the two obstacles captures a portion of the highly energetic flow from the outer part of the boundary layer, and due to the larger available space, the wake of the first obstacle is not conveyed to the second obstacle. Consequently, we observe (i) a horseshoe vortex similar in size to the one observed in front of the first obstacle forms upstream of the second cylinder, (ii) the flow detaches at the roof edge, producing a weaker wake similar to that of the first obstacle, and (iii) the downwash effect behind the obstacle intensifies.

The streamwise (left panels) and vertical (right panels) velocity components for the SF case for two obstacles with AR2 (upfront cylinder) and AR1 (rear cylinder). This case has been denoted as SF21 and it is plotted in the upper panels of Figure 9. On the other hand, the corresponding WI case, denoted as WI21, has been plotted in the bottom panels.

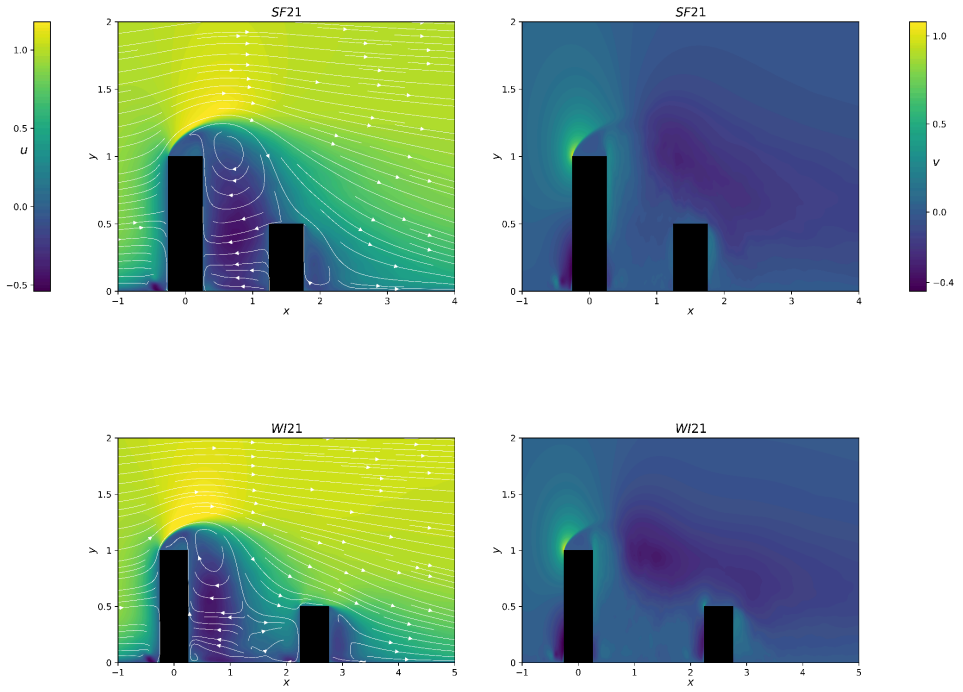

Figure 9: Comparison of the streamwise velocity components from the cases SF21 (upper panels), WI21 (bottom panels). The streamlines are also reported for clarity.

The streamwise velocity is easily compared with the streamwise structures displayed in Figure 8. The gap between the two obstacles is the same for the SF and WI cases reported in Atzori et al. [16]. For the case SF21, the wake of the first obstacle displays two large recirculation bubbles that are more similar to what was observed for the AR2 than the SF case. This is due to the difference in heights of the two cylinders. Although for the SF case, the second obstacle delimits the correct development of the wake of the upfront cylinder, in the case SF21, the wake avoids the second obstacle and passes behind it. The flow reattaches at the roof of the second obstacle. For y > 0.5 the wake correctly develops above the second obstacle. It is worth noting that the second obstacle only affects the bottom portion of the wake and produces a sort of prolongation of the wake that degrades behind the second obstacle. We also note that the second wake is weaker and degrades more quickly downstream when compared to the case SF in Figure 7. In addition, in the case of SF, the larger structures are disrupted by the second cylinder, and the turbulence is thus attenuated. The second cylinder screens the turbulence of the first wake for the entire region behind the second obstacle. Otherwise, this effect is weaker for the

case SF21 since the wake of the first cylinder extends downstream the second obstacle. For the WI21 case, the influence of the rear cylinder is weak and its effect is confined to the bottom part of the wake. In the upper part of the wake, the flow freely develops. In the symmetric plane, the flow reattaches on the roof edge of the second cylinder. This produces a stronger downwash effect (not seen for the isolated cylinder) caused by the tip vortices.

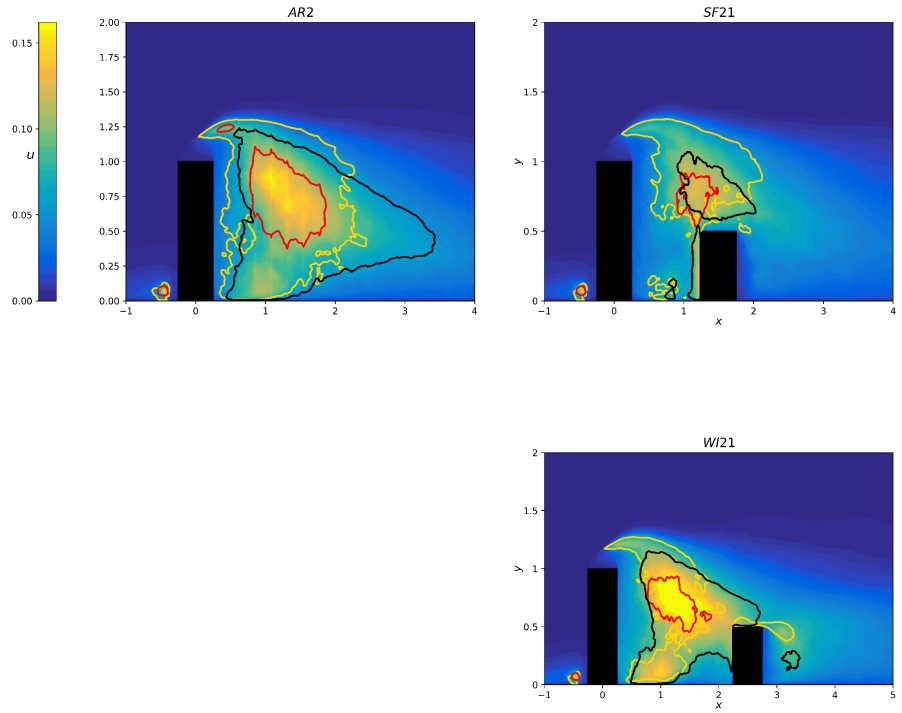

Figure 10: turbulent kinetic energy at the symmetry plane z = 0 for the cases AR2, SF21 and WI21. The contour lines delimit the regions of high $\overline{u'u'}$ (yellow) $\overline{v'v'}$ (red) and $\overline{w'w'}$(black).

The comparison of the turbulent kinetic energy is reported in Figure 10. TKE reaches its maximum between the two obstacles and occupies a large portion of the wake, particularly evident in the case AR2. The presence of the rear obstacle reduces the dimensions of the TKE peak, confining it between the obstacles, as observed in the SF case where both cylinders have equal heights (not depicted here for brevity). However, decreasing the height of the second obstacle results in more space available for the upper portion of the wake to develop, leading to the extension of the TKE region above the second cylinder. Although smaller in size compared to the AR2 case, this extension is more intense and larger than in the corresponding SF case. In addition, the wake of the rear cylinder exhibits distinctions from the case presented by Atzori et al. [16]. The peak region of TKE broadly corresponds to the peak region of streamwise stress $\overline{v'v'}$ for all considered cases. Ahead of the first obstacle, the TKE peak outlines the horseshoe vortex. However, the presence of the second obstacle reduces the size of this peak while maintaining its position. Similarly, the

peak region of $\overline{w'w'}$, initially spanning the entire wake in the AR2 case, extends ahead and above the second obstacle in the SF21 case.

Between the two cylinders, a secondary peak of $\overline{v'v'}$ and $\overline{w'w'}$ is evident, with its intensity increasing with the gap. This region corresponds to the upper part of the wake, creating a distinct area. It is worth noting that the peak of the streamwise stress originates from the edge of the first obstacle, extends between the cylinders, and reaches the area downstream of the rear cylinder. The simulations for the case IR21 are currently running.

7 Training of the DLNN

The unsteady flow from the case SF21 is currently used to train the NN using the DRL method to predict the optimum trajectory of a drone flying from a random point in front of the first obstacle to a random target zone downstream the obstacles. The results of the 3D DNS simulation are processed and fed into Deep Reinforcement Learning (DRL) algorithm. The first approach to develop an efficient learning algorithm starts from a simplified 2D case, so the data have to be appropriately preprocessed. A plane of $z=0$ is extracted from every snapshot of the simulation, so that the fields can be arranged to give a temporal evolution of the flow field. Once all the snapshots have been processed, they are saved in a .h5 file, which can then be fed into the DRL algorithm, which can read the relevant variables of the flow field (e.i. spatial coordinates, velocity of the flow field at each grid point and obstacles positions).

Figure 11 depicts an example of the drone trajectory for the SF21 case. In the present snapshots, the starting point is set before the first obstacle while the arriving region is behind the rear cylinder. The drone avoids the first cylinder by “skimming” the flow. Behind the second obstacle, the drone rapidly drops.

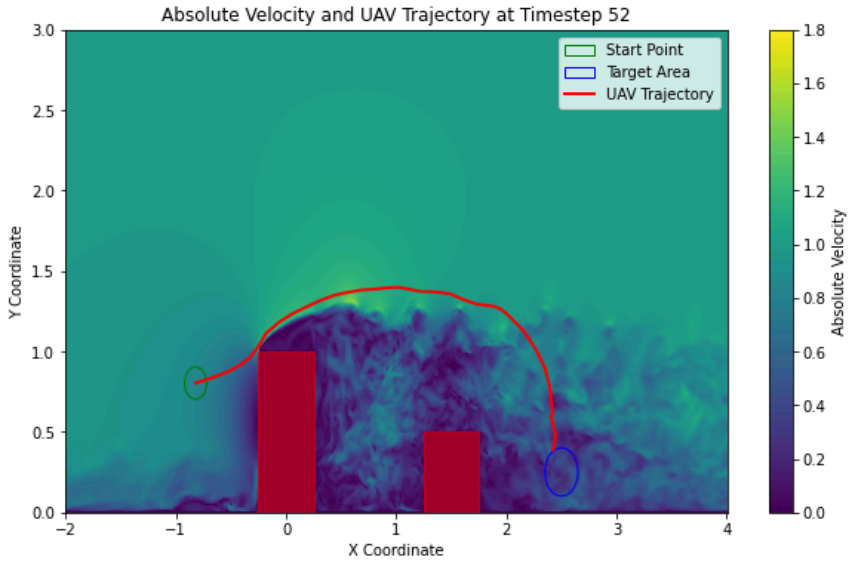

Figure 11: Example of the optimum trajectory predicted by the NN for the case SF21. The green line delimits the starting point while the dark blue circle delimits the arriving region.

8 Conclusions

The increase of urban air traffic presents a significant challenge with the increase of urban population. Despite numerous authors having examined the flow topology surrounding a wall-mounted cylinder [9,12-13,16,29], the primary objective of this study is to elucidate the impact of aspect ratio (AR) and obstacle heights on the wake of a wall-mounted square cylinder within a turbulent boundary layer characterized by a high Reynolds number, employing high-resolution simulations to enhance comprehension of turbulence behavior for a wall-mounted square cylinders in a turbulent boundary layer. Our analysis is conducted at a lower Reynolds number than the actual velocities and length scales observed in urban flows. This limit is justified by the fact that increasing the Reynolds number would impact the computational cost, or make it infeasible to maintain the same accuracy level, making the high-resolution LES setup unfeasible.

The near-wake structures exhibit a large three-dimensional structure, with a large recirculation zone behind the obstacle corresponding to high turbulence production. At the roof, the flow detaches, generating the so-called tip vortices and a strong downwash velocity in the mean flow, while the base vortices are predicted for the quadrupole wake. The presence of a dipole (with only tip vortices) and a quadrupole wake (with both emerging tip and base vortices) strongly affects the performance of the UAVs flying in proximity of the buildings. The instantaneous flow field finally

displays the vortex shedding of the wake for a high aspect ratio, breaking the wake symmetry.

The present study also describes the transition from a dipole to a quadrupole wake configuration that happens for a critical value of AR of 2. Combining the present results with the data published in the literature, we displayed a dependence of the critical AR on the Reθ. However, more databases are still necessary to describe the transition between dipole and quadrupole better wakes. The near-wake configuration and the effect of AR on the TKE budget need a more detailed interpretation when considering their impacts on a real-life operating scenario, since the present study describes a simplified configuration. Unanswered questions, involving the exploration of additional geometric parameters such as cross-section aspect ratio (CR) or the boundary-layer thickness, and the correlation between the TKE budget with the trajectory optimization of drones will be addressed in the future.

These results constitute the first step of a more comprehensive analysis for the controlling and optimising the increasing urban air traffic. In this context, the figures reported from the WP3 are only examples of the potential of the framework developing in the RefMap project.

References

[1] United Nations, (2020), *Cities and Pollution Contribute to Climate Change,* https://www.un.org/en/climatechange/cities-pollution.shtml.Accessedon10September2020, [Date of access 2024-03-22].

[2] United Nations DESA (2022), *The Sustainable Development Goals Report 2022*, United Nations.

[3] Monnier, B., Neiswander, B. and Wark, C. (2010) Stereoscopic particle image velocimetry measurements in an urban-type boundary layer: insight into flow regimes and incidence angle effect, *Boundary-Layer Meteorol*ogy, 135, 243

[4] Britter, R. E. and Hanna, S. R. (2003) Flow and dispersion in urban areas, *Annu. Rev. Fluid Mech.* 35, 469496

[5] Di Sabatino, S., Leo, L. S., Hedquist, B. C., Carter, W. and Fernando, H. J. S. (2009) Results from the Phoenix Urban Heat Island (UHI) experiment: effects at the local, neighbourhood and urban scales, *Eighth Symposium on the Urban Environment, Phoenix, Arizona* (USA)

[6] Britter, R. and Hunt, J. (1979) Velocity measurements and order of magnitude estimates of the flow between two buildings in a simulated atmospheric boundary layer, *J. Wind. Eng. Ind. Aerodyn.,* 4, 165

[7] Oke, T. (1988) Street design and urban canopy layer climate, *Energy Build.,* 11, 103

[8] Torres, P., Le Clainche, S. and Vinuesa, R. (2021) On the experimental, numerical and data-driven methods to study urban flows, *Energies* 14, 10.3390

[9] Zhao, M., Mamoon, A., and Wu, H. (2021) Numerical study of the flow past two wall-mounted finite-length square cylinders in tandem arrangement, *Physics of Fluids,* 33, 093603

[10] Keshavarzian, E., Jin, R., Dong, K. and Kwok, K. C. (2021) Effect of building cross-section shape on air pollutant dispersion around buildings, *Build. Environ.* 197, 107861

[11] Kumar, P. and Tiwari, S. (2019) Effect of incoming shear on unsteady wake in flow past surface mounted polygonal prism, *Physics of Fluids,* 31, 113607

[12] Chen, G., Li, X.-B., Sun, B. and Liang, X.-F. (2022) Effect of incoming boundary layer thickness on the flow dynamics of a square finite wall-mounted cylinder, *Physics of Fluids*, 34, 015105

[13] Wang, H. F. and Zhou, Y. (2009) The finite-length square cylinder near wake, *J. Fluid Mech.,* 638, 453490

[14] Sakamoto, H. and Arie, M. (1983) Vortex shedding from a rectangular prism and a circular cylinder placed vertically in a turbulent boundary layer, *J. Fluid Mech.* 126, 147165

[15] Pattenden, R. J., Turnock, S. R. and Zhang, X. (2005) Measurements of the flow over a low-aspect-ratio cylinder mounted on a ground plane, *Experimental Fluids*, 39, 10

[16] Atzori, M., Torres, P., Vidal, A., Le Clainche, S., Hoyas, S. and Vinuesa, R. (2023) High-resolution simulations of a turbulent boundary layer impacting two obstacles in tandem, *Phys. Rev. Fluids* 8, 063801

[17] Lim, D., Hertwig, D., Grylls, T., Gough, H., van Reeuwijk, M., Grimmond, S. and Vanderwel, C. (2022) Pollutant dispersion by tall buildings: Laboratory experiments and Large-Eddy Simulation. *Experiments in Fluids*, 63, 92

[18] Hertwig D., Gough H.-L., Grimmond S., Barlow J. F., Kent C. W., Lin W. E., Robins A. G., Hayden P. (2019) Wake characteristics of tall buildings in a realistic urban canopy. *Boundary-Layer Meteorol*, 172, 239–270

[19] Grylls T., Le Cornec C. M., Salizzoni P., Soulhac L., Stettler M. E. J., van Reeuwijk M. (2019) Evaluation of an operational air quality model using large-eddy simulation. *Atmos Environ X*, 3, 41

[20] Tolias, I.C., Koutsourakis, N., Hertwig, D. , Efthimiou, G.C., Venetsanos, A.G. and Bartzis, J.G. (2018) Large Eddy Simulation study on the structure of turbulent flow in a complex city. *Journal of Wind Engineering and Industrial Aerodynamics*, 177, 101 - 116

[21] Burman, J., Jonsson, L., Rutgersson, A. (2019) On possibilities to estimate local concentration variations with CFD-LES in real urban environments. *Environ Fluid Mech*, 19, 719–750

[22] Britter, R. E., Hanna, S. R. (2003). Flow and dispersion in urban areas. *Annual review of fluid mechanics*, 35, 469-496

[23] Marucci D, Carpentieri M. (2020) Dispersion in an array of buildings in stable and convective atmospheric conditions. *Atmos Environ*, 222, 100

[24] Grylls, T., Suter, I., Sützl, B., Owens, S., Meyer, D., and van Reeuwijk, M. (2021) uDALES: large-eddy-simulation software for urban flow, dispersion, and microclimate modelling, *J. Open Source Softw.*, 6, 3055.

[25] Suter, I., Grylls, T., Sützl, B. S., Owens, S. O., Wilson, C. E., van Reeuwijk, M. (2022) uDALES 1.0: a large-eddy simulation model for urban environments, *Geosci. Model Dev.*, 15, 5309–5335

[26] Heus, T., van Heerwaarden, C. C., Jonker, H. J. J., Pier Siebesma, A., Axelsen, S., van den Dries, K., Geoffroy, O., Moene, A. F., Pino, D., de Roode, S. R., Vilà-Guerau de Arellano, J. (2010) Formulation of the Dutch Atmospheric Large-Eddy Simulation (DALES) and overview of its applications, *Geosci. Model Dev.*, 3, 415–444.

[27] Shin, H. H., D. Muñoz-Esparza, J. A. Sauer, and M. Steiner, 2021: Large-Eddy Simulations of Stability-Varying Atmospheric Boundary Layer Flow over Isolated Buildings. J. Atmos. Sci., 78, 1487–1501

[28] García-Sánchez, C., van Beeck, J., Gorlé, C. (2018) Predictive large eddy simulations for urban flows: Challenges and opportunities, *Building and Environment*, 139, 146-156,

[29] Wang, H. F. and Zhou, Y. (2009) The finite-length square cylinder near wake, *J. Fluid Mech.* 638, 453490

[30] Sakamoto, H. and Arie, M. (1983) Vortex shedding from a rectangular prism and a circular cylinder placed vertically in a turbulent boundary layer, *J. Fluid Mech.* 126, 147165

[31] Sumner, D. Heseltine, D. and Dansereau, O. (2004) Wake structure of a finite circular cylinder of small aspect ratio, Exp. Fluids 37, 720

[32] Rastan, M. Shahbazi, H., Sohankar, A., Mahbub Alam, Md., and Zhou, Y. (2021) The wake of a wall-mounted rectangular cylinder: Cross-sectional aspect ratio effect, *J. Wind. Eng. Ind. Aerodyn.* 213, 104615

[33] Saeedi, M. LePoudre, P. P. and Wang, B. C. (2014) Direct numerical simulation of turbulent wake behind a surface-mounted square cylinder, *J Fluids Struct* 51, 2039

[34] Tian, G. Conan, B. and Calmet, I. (2021) Turbulence-kinetic-energy budget in the urban-like boundary layer using large-eddy simulation, *Bound.-Layer Meteorol.* 178, 201

[35] Corke, T. C. Nagib, H. M. and Tan-Atichat, J. (1979) Flow near a building model in a family of surface layers, *J. Wind Eng. Ind. Aerodyn.* 5, 139

[36] Fischer, P., Lottes, J. and Kerkemeier, S. (2008) *Nek5000: Open source spectral element cfd solver*, https://nek5000.mcs.anl.gov/ [Date of access 2024-03-22]

[37] Patera, A. T. (1984) A spectral element method for fluid dynamics: Laminar flow in a channel expansion, *J. Comput. Phys.* 54, 468

[38] Negi, P., Vinuesa, R., Hanifi, A., Schlatter, P. and Henningson, D. (2018) Unsteady aerodynamic effects in small-amplitude pitch oscillations of an airfoil, *International Journal of Heat and Fluid Flow* 71, 378391.

[39] Dong, S., Karniadakis, G., and Chryssostomidis, C. (2014) A robust and accurate outflow boundary condition for incompressible flow simulations on severely-truncated unbounded domains, *J. Comput. Phys.* 261, 83

[40] Zhang, D. Cheng, L. An, L. and Zhao, M. (2017) Direct numerical simulation of flow around a surface-mounted finite square cylinder at low Reynolds numbers, *Phys. Fluids* 29, 045101

[41] Dousset, V. and Pothrat, A. (2010) Formation mechanism of hairpin vortices in the wake of a truncated square cylinder in a duct, *J. Fluid Mech.* 653, 519536

[42] Yauwenas, Y. Porteous, R. Moreau, D. J. and Doolan, C. J. (2019) The effect of aspect ratio on the wake structure of finite wall-mounted square cylinders, *J. Fluid Mech.* 875, 929960

[43] Vinuesa, R. Schlatter, P. Malm, J. Mavriplis, C. and Henningson, D. S. (2015) Direct numerical simulation of the flow around a wall-mounted square cylinder under various inflow conditions, *J. Turb.* 16, 555587

[44] Hosseini, Z. Bourgeois, J. A. and Martinuzzi, R. J. (2013) Large-scale structures in dipole and quadrupole wakes of a wall-mounted finite rectangular cylinder, *Exp. Fluids* 54, 1595

[45] Bourgeois, J. A. Sattari, P. and Martinuzzi,R. J. (2011) Alternating half-loop shedding in the turbulent wake of a finite surface-mounted square cylinder with a thin boundary layer, *Phys. Fluids* 23, 095101

[46] Sattari, P. Bourgeois, J. A. and Martinuzzi, R. J. (2012) On the vortex dynamics in the wake of a finite surface-mounted square cylinder, *Exp. Fluids* 52, 1149

[47] Uffinger, T. Ali, I. and Becker, S. (2013) Experimental and numerical investigation of the flow around three different wall-mounted cylinder geometries of finite length, *J. Wind. Eng. Ind. Aerodyn.* 119, 13